HHS Public Access

Author manuscript

J Phys Chem Lett. Author manuscript; available in PMC 2021 July 10.

Published in final edited form as:

J Phys Chem Lett. 2021 March 25; 12(11): 2712–2720. doi:10.1021/acs.jpclett.1c00094.

Elucidating the Electronic Structure of a Delayed Fluorescence Emitter via Orbital Interactions, Excitation Energy Components, Charge-Transfer Numbers, and Vibrational Reorganization Energies

Zheng Pei[#†], **Qi Ou**[#‡], **Yuezhi Mao**[¶], **Junjie Yang**[§], **Aurélien de la Lande**[‖], **Felix Plasser**[⊥], **Wanzhen Liang**[†], **Zhigang Shuai**[‡], **Yihan Shao**[§]

[†]State Key Laboratory of Physical Chemistry of Solid Surfaces, Collaborative Innovation Center of Chemistry for Energy Materials, Fujian Provincial Key Laboratory of Theoretical and Computational Chemistry, and Department of Chemistry, College of Chemistry and Chemical Engineering, Xiamen University, Xiamen 361005, P. R. China.

[‡]MOE Key Laboratory of Organic OptoElectronics and Molecular Engineering, Department of Chemistry, Tsinghua University, Beijing 100084, China.

[¶]Department of Chemistry, Stanford University, Stanford, CA 94305, United States.

[§]Department of Chemistry and Biochemistry, University of Oklahoma, Norman, OK 73019, United States.

[‖]Laboratoire de Chimie Physique, Université Paris Sud, CNRS, Université, Paris Saclay. 15 avenue Jean Perrin, F91405 Orsay, France

[⊥]Department of Chemistry, Loughborough University, Loughborough, LE11 3TU, United Kingdom

[#] These authors contributed equally to this work.

Abstract

Recently, Wang and coworkers carried out frontier molecule orbital engineering in the design of *m*-Cz-BNCz, a thermally-activated delayed fluorescence (TADF) molecule that emits pure green light at an external quantum efficiency of 27%. To further understand the underlying molecular design principles, we employed four advanced electronic structure analysis tools. Firstly, an absolutely localized molecular orbitals (ALMO)-based analysis indicates an anti-bonding combination between the highest occupied molecular orbitals (HOMOs) of the donor 3,6-di-*tert*-butylcarbazole fragment and the acceptor BNCz fragment, which raises the HOMO energy and red-shifts the fluorescence emission wavelength. Secondly, excitation energy component analysis reveals that the S_1–T_1 gap is dominated by two-electron components of the excitation energies. Thirdly, charge transfer number analysis, which is extended to use fragment-based Hirshfeld

qiou@tsinghua.edu.cn; yuezhi.mao@stanford.edu; f.plasser@lboro.ac.uk; liangwz@xmu.edu.cn; zgshuai@tsinghua.edu.cn; yihan.shao@ou.edu.

Supporting Information Available: Details of the charge-transfer number calculation schemes and excitation energy decomposition methods; numerical results from BNCz, *m*-Cz-BNCz, and *p*-Cz-BNCz calculations, including charge-transfer numbers, excitation energy components, spin-orbit couplings, estimated transition rates, and solvation and geometry effects; coordinates of optimized geometries. This material is available free of charge via the Internet at http://pubs.acs.org/.

weights, indicates that the S_1 and T_1 excited states of *m*-Cz-BNCz (within time-dependent density functional theory) have notable charge transfer characters (27% for S_1 and 12% for T_1). This provides a balance between a small single-triplet gap and a substantial fluorescence intensity. Lastly, a vibrational reorganization energy analysis pin-points the torsional motion between the BNCz and Cz moieties of *m*-Cz-BNCz as the source for its wider emission peak than that of *p*-Cz-BNCz. These four types of analyses are expected to be very valuable in the study and design of other TADF and functional dye molecules.

Graphical Abstract

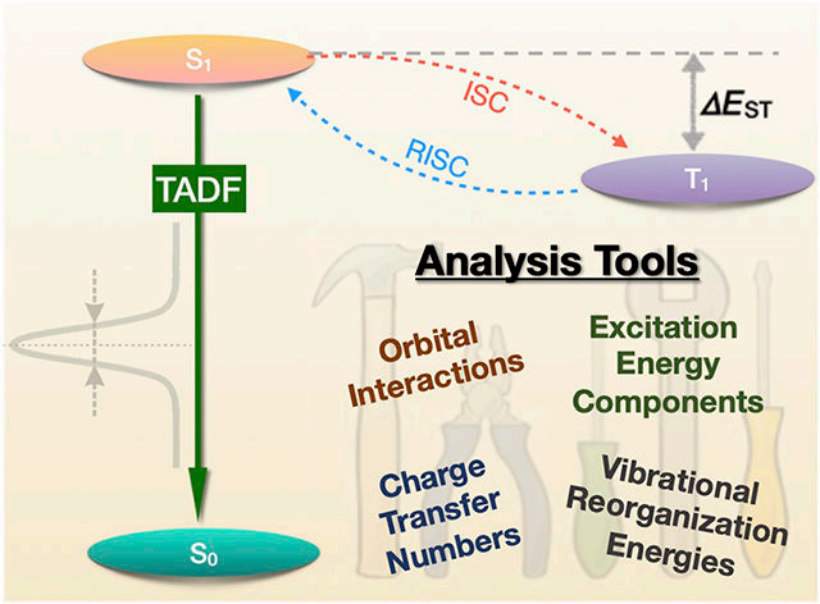

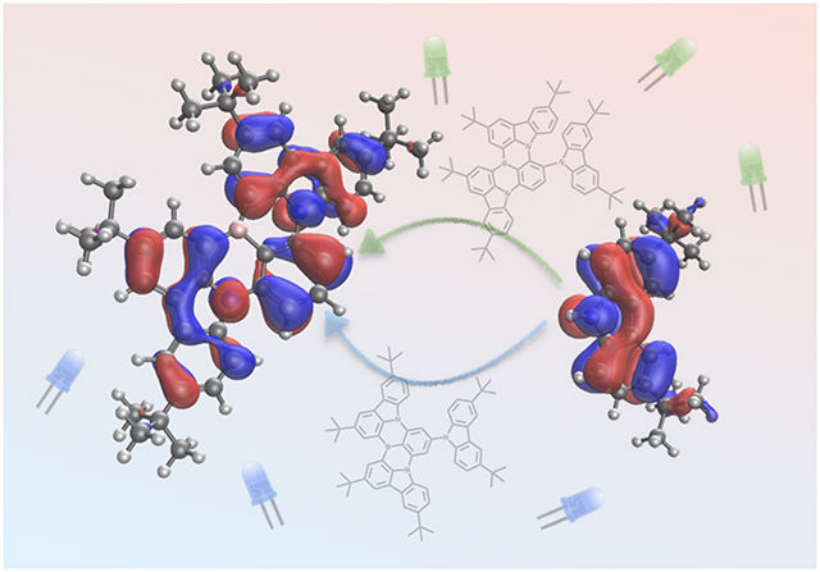

Thermally activated delayed fluorescence (TADF) materials, which are known as the third generation of organic electroluminescent materials, can harvest all the current-generated

singlet and triplet excitons for fluorescence and achieve a 100% internal quantum efficiency (IQE).[1-5] Key to the occurrence of the delayed fluorescence is an efficient reverse intersystem crossing (RISC) process within a TADF molecule, which requires a relatively small energy gap and a large spin-orbit coupling (SOC) between the S_1 and T_1 states.[6-8] Minimized S_1–T_1 energy gap can be achieved through a pair of marginally overlapped frontier orbitals, and thus many earlier TADF molecules were developed with a twisted intramolecular charge-transfer (TICT) character.[9-13] However, because of the dominating CT transition of S_1 back to S_0, the emission spectra of such twisted TADF molecules are usually severely broadened (with a full-width at half maximum (FWHM) around 70–100 nm), thus failing to provide the desired purity for high-resolution displays.[14-17]

A dedicated design strategy, known as multi-resonance induced TADF (MR-TADF), has been reported by Hatakeyama *et al.* in 2016.[18] Within this strategy, electron-deficient atoms (such as boron) and electron-rich atoms (such as nitrogen) are oppositely placed in a rigid polycyclic aromatic framework, rendering the frontier orbitals effectively separated via multiple resonance effects. A series of MR-TADF molecules have been designed and synthesized, with extremely narrow bandwidth (FWHM around 20 nm) and excellent electroluminescent performance.[19-23] Nevertheless, due to the structural similarity, most of the reported MR-TADF molecules are blue-light emitters.[18-22] This has inspired the development of MR-TADF molecules with other emission wavelengths.

An exciting breakthrough of MR-TADF materials with green emission was reported recently by Wang and co-workers via frontier molecular orbital engineering (FMOE). [24] The target molecule, *m*-Cz-BNCz (shown in Figure 1), which combines a B–N containing MR frame (BNCz) with a 3,6-di-*tert*-butylcarbazole substituent (DtBuCz, shortened as “Cz” in this Letter), was successfully employed as an emitter to fabricate pure green organic light-emitting diodes (OLEDs) with a maximum external quantum efficiency (EQE) of 27%. In contrast, the *p*-Cz-BNCz isomer emits blue light.

To fully understand the remarkable performance of the *m*-Cz-BNCz emitter, additional theoretical insights of its electronic structural and photophysical properties are needed, especially the cause of the red-shifted spectra compared to its para-substituent isomer, *p*-Cz-BNCz. This will be achieved in this Letter by employing four latest electronic structure analysis tools.

ALMO-Based Orbital Interactions Analysis.

To decipher the difference in the electronic structural and photophysical properties of *m*-Cz-BNCz and *p*-Cz-BNCz, we divide these complexes into two fragments, BNCz and Cz, which are linked together by a C—N bond. A quantitative analysis of interactions between orbitals on covalently linked fragments in a molecular complex was developed by Mao and coworkers, [25] which allows us to go beyond a qualitative interpretation of the frontier orbitals of these complexes and quantify their key fragment contributions. This analysis is built upon the ALMO analysis from the Head-Gordon group[26-30] and closely resembles the *in-situ* block-localized wavefunction analysis from Mo and coworkers. [31-34] Here we shall briefly outline our analysis procedure implemented within a development version of Q-Chem

5.2.[35] To properly describe excited states with a partial charge-transfer character, we employ LRC-ωPBE,[36,37] a range-separated hybrid functional, with an optimally tuned ω value obtained for each molecule following the procedure in Ref. 38. This functional was reported to best describe the electronic structure of TADF molecules within the TDDFT framework of theory. [39,40]

- Step I. Build the "isolated" state by constructing isolated fragments and obtaining their respective fragment orbitals. For covalently linked fragments, such as those in *m*-Cz-BNCz and *p*-Cz-BNCz, the main fragment (BNCz) can be terminated with a hydrogen link atom, while the attached fragment (Cz) can be saturated with a benzene ring. Standard self-consistent field (SCF) calculations are performed for each saturated fragment. Orbital localization is then carried out to identify (i) the C—H bond orbital in BNCz–H associated with the hydrogen link atom; and (ii) the bridge C—N bond orbital and benzene orbitals of Cz–Ph. SCF calculations are then performed again with the identified bond orbitals frozen to obtain the other orbitals that are truncated and "absolutely localized" on fragments, $\psi_{xp}^{\mathrm{FRAG}}$.
- Step II. Construct the "frozen" state. Fragment orbitals are combined together without relaxation ($\psi_{xp}^{\mathrm{FRZ}} = \psi_{xp}^{\mathrm{FRAG}}$) and then antisymmetrized to obtain a "frozen" state. Its difference from the "isolated" state corresponds to the effects of permanent electrostatics and exchange-repulsion on the frontier orbitals.
- Step III. Construct the "polarized" state (also called the ALMO state). Two sets of fragment orbitals are allowed to polarize each other while restricted to stay localized on each fragment. This leads to the "polarized" state of the system with fully polarized fragment orbitals, ψ_{xp}^{POL}.
- Step IV. Analyze the interaction between polarized fragment orbitals. This is done by projecting the conventional MOs, ψ_{p}^{FULL}, onto the polarized fragment orbitals,

$$\left|\psi_{q}^{\mathrm{FULL}}\right\rangle = \sum_{xp} Y_{q}^{xp} \left|\psi_{xp}^{\mathrm{POL}}\right\rangle \tag{1}$$

$$Y_{q}^{xp} = \left\langle \psi^{xp,\mathrm{POL}} \middle| \psi^{xp,\mathrm{POL}} \right\rangle \psi_{q}^{\mathrm{FULL}} \tag{2}$$

Note that contravariant fragment orbitals,[26,41] $\psi^{xp,\mathrm{POL}} = \sum_{x'p'} (S^{-1})^{xp,x'p'} \psi_{x'p'}^{\mathrm{POL}}$, are used to ensure proper projections within the space spanned by two sets of fragment MOs, which are non-orthogonal to each other with an overlap $S_{xp,x'p'} = \left\langle \psi_{xp}^{\mathrm{POL}} \middle| \psi_{x'p'}^{\mathrm{POL}} \right\rangle$.

m-Cz-BNCz.

As illustrated in Fig. 2, the HOMO of the complex, *m*-Cz-BNCz, is composed by HOMOs from both the donor (Cz) and acceptor (BNCz), with mixing coefficients 0.76 and 0.63,

respectively. *Across the C—N bond between the two fragments, the phase of the HOMO changes from red (on BNCz carbon) to blue (on Cz nitrogen), which indicates an anti-bonding (destructive) combination.* Such an anti-bonding combination raises the (nearly degenerate) fragment HOMO energies of −6.517 eV (BNCz) and −6.517 eV (Cz) to the value of −6.216 eV for the *m*-Cz-BNCz complex.

In contrast, the LUMO of the BNCz fragment contributes exclusively to the LUMO of the complex, with its orbital energy increased slightly from −1.133 to −1.066 eV. This is also confirmed by the fragment and complex LUMOs in the figure, which looks essentially identical. In general, a substantial overlap between orbitals from different fragments is needed for them to interact strongly and mix together. Clearly, the BNCz LUMO has a nearly zero overlap with Cz HOMO because of their different symmetry around the C—N bond. BNCz LUMO also has a very small overlap with Cz LUMO (shown on the top right of Fig. 2), as they are spatially separated.

Putting these together, less energy is needed to excite an electron from an elevated HOMO into a largely unchanged LUMO, causing a red-shift in the HOMO→LUMO excitation compared to BNCz.

p-Cz-BNCz.

For the para-substituted isomer, as depicted in Fig. 3, both its HOMO and LUMO come directly from the BNCz fragment, while the Cz fragment has little role in the composition of complex's two frontier orbitals. This suggests that both the HOMO and LUMO remained localized on the BNCz fragment, with the corresponding energies raised marginally by 0.096 and 0.228 eV, respectively. Specifically, the BNCz HOMO (shown on the bottom left of Fig. 3) and Cz HOMO (similar to the one on the bottom right of Fig. 2) have different symmetry around the C—N bond of the para-substituted isomer. *A nearly zero overlap between the HOMOs prevents a strong interaction between and a mixing of the two orbitals.* On the other hand, the slightly larger increase in the LUMO energy arises from a very small anti-bonding contribution from the nitrogen atom of the Cz fragment, which agrees with the experimentally observed small blue shift in the emission energy.

When it comes to FMOE, the Cz substitution group behaves like an electron donating group (EDG), whose HOMO has a considerable weight on the nitrogen atom. To exert a noticeable effect on the fluorophore electronic properties, the HOMO of an EDG needs to be mixed into the fluorophore HOMO (with a similar energy) and with a linkage that allows a substantial overlap between the fluorophore and substituent HOMOs. As the BNCz fluorophore HOMO has a much larger weight on the meta site than on the para site, only a linkage at the meta-site leads to a "head-on" overlap between the two orbitals and consequently a substantial increase of the HOMO energy.

Excitation Energy Component Analysis.

The ALMO-based frontier orbital analysis above provides a theoretical basis for the narrowing of HOMO-LUMO gap in *m*-Cz-BNCz (compared to BNCz) as well as a slightly wider HOMO-LUMO gap in *p*-Cz-BNCz. However, to gain a quantitative understanding of

shifts in fluorescence energies and singlet-triplet splittings, it is expedient to venture beyond the HOMO-LUMO picture and consider other components of the excitation energy. To do so, we decompose the excitation energies into a sum of four 1-electron terms and three 2-electron terms, as described in Refs. 42 and 43. For the first six vertical excitation energies for each molecule (at corresponding S_0 geometries), the results are shown in Fig. 4 while the full underlying numerical data of all seven terms is provided in Table S10. Within the TDDFT-TDA theory, the S_1 excitation energies are: 2.719 eV (*m*-Cz-BNCz) < 2.975 eV (BNCz) < 2.996 eV (*p*-Cz-BNCz), which follows exactly the trend as the observed emission wavelengths. The 2-electron contributions to the S_1 excitation energies (shown as the red bars in Fig. 4 due to their negative values) are clearly very similar across these systems, with numerical values of −2.640, −2.893, and −2.741 eV, respectively. In contrast, the 1-electron contributions (shown as the blue bars in Fig. 4) are 5.358 eV (*m*-Cz-BNCz), 5.868 eV (BNCz), and 5.737 eV (*p*-Cz-BNCz), which are primarily responsible for the difference between the computed excitation energies. *This reaffirms the validity of our ALMO-based frontier orbital-interactions analysis in interpreting spectral shifts.*

TDDFT-TDA calculations predict the vertical S_1–T_1 energy gaps[44] to be 0.404 eV (*m*-Cz-BNCz) < 0.475 eV (*p*-Cz-BNCz) < 0.483 eV (BNCz), which should facilitate RISC for *m*-Cz-BNCz. Explaining the S_1–T_1 gaps based on the HOMO-LUMO gaps is not possible considering that all S_1 and T_1 states are dominated by the HOMO-LUMO transition and an analysis of the 2-electron terms is unavoidable. Indeed, Fig. 4 demonstrates that the S_1–T_1 energy gaps are primarily caused by the 2-electron components. Traditionally, the splitting between S_1 and T_1 is explained via the exchange integral between HOMO and LUMO[11] and this term can be generalized as the self-repulsion of the transition density evaluated as a 2-electron component of the excitation energy. [42] This term destabilizes singlets but has no effect on triplets and, thus, increases the gap between them. (Note that, with global or range-separated hybrid functionals, a similar term with a scaled or range-separated Coulomb operator contributes to the Hartree-Fock exchange component of the unoccupied orbital energies and would thus stabilize both S_1 and T_1 through the orbital energy difference component of the excitation energy.[45]) Within TDDFT this term arises from the response of the Coulomb matrix and is denoted “J2” here. Interestingly, the “J2” terms account for only half the overall splittings: 0.239 eV for BNCz, 0.229 eV for *p*-Cz-BNCz, and 0.173 eV for *m*-Cz-BNCz. The remaining energy is distributed among the 1-electron term, the 2-electron response of the non-local exchange “K2”, and the 2-electron response of the XC-functional “XC2.” This discussion highlights that, while “J2” can be the dominant term of the vertical S_1–T_1 energy gaps, a quantitative prediction of excitation energies requires the consideration of one-electron and other two-electron contributions.

One finds that the “J2” component is larger with local excitations (*e.g.* 0.239 eV for BNCz and 0.229 eV for *p*-Cz-BNCz) than with partially charge-transfer excitations (*e.g.* 0.173 eV for *m*-Cz-BNCz). (The character of these excitations (local excitation *vs* charge-transfer) are quantified using the charge-transfer number analysis[42,46,47] shown below.) The “K2” component of the excitation energy, which comes from the response of the Hartree-Fock exchange matrix, is always negative and therefore stabilizes both the singlet and triplet states. “K2” can be interpreted as the Coulomb binding between the electron and hole quasiparticles[42,48] and is larger for tightly bound local excitations than for loosely bound

charge-transfer excitations. This underlies the less negative "K2" value (−2.775 eV) for the 27%-CT S_1 state of *m*-Cz-BNCz than BNCz (−3.082 eV) and *p*-Cz-BNCz (−2.921 eV). Similarly, the 12%-CT T_1 state of *m*-Cz-BNCz also had a slightly less negative "K2" value (−2.944 eV) than BNCz (−3.214 eV) and *p*-Cz-BNCz (−3.038 eV).

Charge-Transfer Number Analysis.

The charge-transfer number analysis was proposed by Plasser and coworkers.[42,46,47] For the *I*-th TDDFT-TDA excited state, the particle-hole transition density matrix can be expressed as

$$\gamma_{0I}(r_e, r_h) = \sum_{ai} X_{ai}^I \psi_a(r_e)\psi_i(r_h) \tag{3}$$

where $\mathbf{X}_{ai}^I$ refers to the transition amplitudes for exciting an electron from the *i*-th occupied orbital into the *a*-th unoccupied orbital. The particle-hole transition density matrix is normalized.

$$\begin{aligned} &\int \mathrm{d}r_e \mathrm{d}r_h \mid \gamma_{0I}(r_e, r_h) \mid^2 \\ &= \sum_{ai,bj} X_{ai}^I X_{bj}^I \left[\int \psi_i^*(r_h)\psi_j(r_h)\mathrm{d}r_h\right]\left[\int \psi_a^*(r_e)\psi_b(r_e)\mathrm{d}r_e\right] \\ &= \sum_{ai,bj} X_{ai}^I X_{bj}^I S_{ij} S_{ab} = \sum_{ai,bj} X_{ai}^I X_{bj}^I \delta_{ij}\delta_{ab} = \sum_{ai}\left(X_{ai}^I\right)^2 = 1 \end{aligned} \tag{4}$$

When one decomposes the overlap between occupied (unoccupied) orbitals into fragment contributions,

$$S_{ij} = \delta_{ij} = \sum_F \widetilde{S}_{ij,F} \tag{5}$$

$$S_{ab} = \delta_{ab} = \sum_{F'} \widetilde{S}_{ab,F'} \tag{6}$$

the charge-transfer numbers can be defined as,

$$\Omega_{F,F'} = \sum_{ai,bj} X_{ai}^I X_{bj}^I \widetilde{S}_{ij,F}\widetilde{S}_{ab,F'} \tag{7}$$

which represent the percentage contribution from the charge-transfer excitation ($F \neq F'$) and local excitation ($F = F'$).

Different fragment partitioning schemes, such as Mulliken, Löwdin, and fragment-based Hirshfeld (FBH), are employed to compute the fragment $S_{ab,F}$ and $S_{ij,F}$ matrices, whose calculations are detailed in Section S1.1 of the Supporting Information (SI).

m-Cz-BNCz.

For the meta-substituted isomer, the charge transfer numbers are computed for the lowest three singlet and triplet excited states using Eq. 7. Their values are tabulated in Table S1 of the SI and FBH values are illustrated in Fig. 5(a). The S_1 state, which is dominated by the HOMO→LUMO excitation (amplitude: 0.9611) and has a vertical excitation energy of 2.7182 eV, is shown to be a mixed local excitation (LE) / charge transfer (CT) state, with 71.61% (within the FBH population scheme) from a local excitation within BNCz; 21.72% from a charge transfer excitation from Cz to BNCz; and minor contributions from reverse charge transfer (0.74%) and local excitation within Cz (0.43%). The T_1 state involves both HOMO→LUMO (amplitude: 0.9070) and HOMO-1→LUMO (amplitude: 0.3347) transitions. Since HOMO-1 is localized on the BNCz fragment, the T_1 state has a larger LE contribution (86.64% within the FBH population scheme) and a smaller CT contribution (12.39%).

In Fig. 5(a), the charge transfer numbers for higher excited state indicate that both T_2 and T_3 are dominated by LE (94.86% and 88.77%, respectively), while S_2 and S_3 are mixed LE/CT states (with 38.73% and 70.69% of LE, respectively). The differences in state characters can be understood in terms of the interplay between the “K2” and “J2” terms, discussed above. Singlets experience short-range exchange repulsion via “J2” and long-range Coulomb attraction via “K2” whereas triplets only experience the attractive “K2” term.[42] As a consequence, one finds that low-energy triplet states are generally more confined, have reduced CT character and enhanced binding energies when compared to related singlet states[8,42,49] (see Section S2.2 of the SI for more details).

In general, the different LE/CT ratios in S_1 and T_1–T_3 are important for efficient RISC processes, as they facilitate larger spin-orbit coupling[50,51] (see Table S17) and vibronic coupling.[52,53] Note that, with T_2 and T_3 close in energy with the S_1 state, they might also play a role in the TADF process of *m*-Cz-BNCz. Within the thermal vibrational correlation function (TVCF) rate formalism,[54] the T_2–T_1 transition rate is estimated to be ultrafast at 10^{13} s^{-1} (see Table S18), suggesting that the RISC should be mainly from T_1. Further spin-vibronic studies on the roles of the T_2 and T_3 states will be pursued following strategies in Refs. 55 and 56.

A detailed comparison of the different population analysis schemes is shown in Table S1. At first sight, it appears surprising that the different population analysis schemes yield almost identical results in Table S1, even though a triple-zeta 6-311G(d,p) basis is used and Mulliken populations are known to be rather sensitive to the basis set size. However, it should be kept in mind that the charge-transfer numbers are computed as a sum over a whole molecular fragment and the population analysis scheme should only affect the atoms immediately adjacent to the bond between the fragments.

p-Cz-BNCz.

For this isomer, the charge transfer numbers of its lowest excited states, as collected in Table S2 of the SI, reveal a very different picture for the lowest singlet and triplet states. Now, both the S_1 and T_1 states are dominated by LE as shown in Fig. 5(b), with the corresponding

charge transfer numbers around 96%. This is expected because both the HOMO and LUMO of *p*-Cz-BNCz are shown to be localized on the BNCz moiety (Fig. 3).

Among the higher-energy excited states of *p*-Cz-BNCz, S_2 has a mixed LE and CT character, in which the weights of CT are 66%. In contrast, T_2, T_3, and S_3 are dominated by LE (larger than 94%).

Vibrational Reorganization Energy Analysis.

The broadening of the absorption/photoluminescence spectra is closely related to the reorganization energy between the light-emitting state and the ground state of a given system.[57] As proposed by Reimers in 2001, within the harmonic oscillator approximation, the total reorganization energy of a system can be evaluated via normal-mode analysis as[58]

$$\lambda = \sum_i \lambda_i = \sum_i \frac{1}{2}\omega_i^2 \Delta Q_i^2 \tag{8}$$

where λ_i corresponds to the reorganization energy due to normal mode i with frequency ω_i, and ΔQ_i represents the displacement along the i-th normal mode coordinate between the equilibrium position of the light-emitting state and the ground state. ΔQ_i can be further expressed as a linear combination of the internal coordinates,

$$\Delta Q_i = \sum_j \alpha_{ij} \Delta S_j \tag{9}$$

where ΔS_j corresponds to the displacement along the jth internal coordinate between the equilibrium position of the light-emitting state and the ground state. Substituting Eq. 9 into Eq. 8, one obtains the reorganization energy with respect to each internal coordinate,

$$\lambda = \sum_j \lambda_j + \sum_{k \neq j} \lambda_{jk} = \sum_{ij} \frac{\omega_i^2}{2}\left(\alpha_{ij}^2 \Delta S_j^2 + \sum_{k \neq j} \alpha_{ij}\alpha_{ik} \Delta S_j \Delta S_k\right) \tag{10}$$

Here, $\lambda_j \equiv \sum_i (\omega_i^2 / 2)\alpha_{ij}^2 \Delta S_j^2$ corresponds to the diagonal elements and $\lambda_{jk} \equiv \sum_i (\omega_i^2 / 2)\alpha_{ij}\alpha_{ik} \Delta S_j \Delta S_k$ corresponds to the off-diagonal elements.

To further validate the role played by the 3,6-di-*tert*-butylcarbazole (Cz) group in *m*-Cz-BNCz, we carry out the reorganization energy analysis between the S_0 and S_1 states (each optimized at the B3LYP/6-31G(d) level of theory) for both *m*-Cz-BNCz and *p*-Cz-BNCz using the molecular material property prediction package MOMAP 2020A.[59-61] As shown in Fig. 6(a) and (b), the reorganization energy of *m*-Cz-BNCz is significantly larger compared to that of *p*-Cz-BNCz, corresponding to a larger $S_1 \rightarrow S_0$ structural change of *m*-Cz-BNCz compared to its para-substituted counterpart. The extra flexibility of *m*-Cz-BNCz structure during its fluorescence lifetime mainly arises from the torsion between the center BNCz moiety and the carbazole group as indicated in Fig. 6(c) and (d). For *m*-Cz-BNCz, the projected reorganization energies onto the dihedral angle between BNCz and Cz moieties are significant, while the corresponding parts in *p*-Cz-BNCz are negligible. The projected

reorganization energies of these two molecules also underline the fact that the S_1 state of *m*-Cz-BNCz has a marked charge-transfer character while the S_1 state of *p*-Cz-BNCz is LE-dominating, which is consistent with the results of charge-transfer number analysis shown in Fig. 5.

The theoretical absorption and photoluminescence spectra can be evaluated via TVCF method as[54]

$$\sigma_{\text{abs}} = \frac{4\pi^2\omega}{3c} \sum_{v_i, v_f} P_{\text{i}v_i}(T) \mid \langle \Theta_{\text{f}v_f} \mid \overrightarrow{\mu}_{\text{fi}} \mid \Theta_{\text{i}v_i} \rangle \mid^2 \times \delta\left(\hbar\omega - E_{\text{fi}} - E_{\text{f}v_f} + E_{\text{i}v_i}\right) \tag{11}$$

$$\sigma_{\text{emi}} = \frac{4\omega^3}{3c^3} \sum_{v_i, v_f} P_{\text{i}v_i}(T) \mid \langle \Theta_{\text{f}v_f} \mid \overrightarrow{\mu}_{\text{fi}} \mid \Theta_{\text{i}v_i} \rangle \mid^2 \times \delta\left(E_{\text{if}} - E_{\text{f}v_f} + E_{\text{i}v_i} - \hbar\omega\right) \tag{12}$$

where $P_{\text{i}v_i}(T)$ is the Boltzmann distribution function for the initial vibronic manifold; $\Theta_{\text{i}_{\text{v}_\text{i}}}$. and $\Theta_{\text{f}_{\text{vf}}}$ are vibrational wavefunctions; E_{fi} (E_{if}) is the adiabatic energy gap between initial (final) and final (initial) electronic states; $E_{\text{i}v_i}$ and $E_{\text{f}v_f}$ are vibraional energies in the corresponding electronic states.

The absorption and photoluminescence spectra of *m*-Cz-BNCz and *p*-Cz-BNCz predicted via the TVCF formalism using MOMAP2020A are given in Fig. 6(e) and 6(f). Due to the larger reorganization energy from the torsion between the BNCz and Cz moieties in *m*-Cz-BNCz, broader spectra are obtained compared to those of *p*-Cz-BNCz. The engagement of CT in the S_1 state of *m*-Cz-BNCz also shifts the emission spectrum bathochromically to green light region, which distinguishes *m*-Cz-BNCz from other blue-light DABNA derivatives. Note that even though the emission spectrum of *m*-Cz-BNCz is broader compared to that of *p*-Cz-BNCz, its 43 nm full-width at half-maximum (FWHM) according to the experimental result still makes it one of the purest green light-emitting complexes among various types of TADF materials.

Before concluding, we briefly want to discuss two methodological aspects: possible influences by the solvent environment and by the density functional. While the orbital interactions, excitation energy components, and charge transfer numbers are analyzed using the LRC-ωPBE functional for gas-phase molecules at their ground-state geometries, all results stay qualitatively the same upon the incorporation of solvent effects or with the adoption of different geometries and functionals. Indeed, a TDDFT/LR-PCM description of the toluene solvent leads to very similar charge transfer numbers in Tables S3 and S4 (compared to Tables S1 and S2) and excitation energy components in Table S11 (versus gas-phase results in Table S10). A more sophisticated TDDFT/ptSS-PCM treatment[62] leads to rather small changes (< 0.1 eV) to the vertical excitation energies, as is evident in Table S14. Ground and excited-state energies in Table S19 of *m*-Cz-BNCz and *p*-Cz-BNCz at different geometries, together with charge transfer numbers of *p*-Cz-BNCz in Table S9 and its excitation energy components in Table S10 at its optimized S_1 structure, indicate that our

analysis results vary only slightly with the molecular geometry. As far as functional is concerned, the use of the B3LYP functional yields an expected more substantial charge-transfer character for the S_1 and T_1 states of *m*-Cz-BNCz, while retaining largely locally excited S_1 and T_1 states for *p*-Cz-BNCz (see Table S5-S8). We caution that, although optimally tuned LRC-ωPBE well reproduced S_1–T_1 gaps for many other TADF molecules,[39,40] the corresponding adiabatic S_1–T_1 gap is predicted to be 0.42 eV for *m*-Cz-BNCz (Table S19), which is much larger than the reported experimental value of 0.08 eV.[24] This reaffirms the recently reported difficulty of TDDFT methods in accurately predicting singlet-triplet gaps for boron-rich MR-TADF molecules,[63] a phenomenon that has been linked to intricate dielectric stabilisation effects.[50]

To summarize, in this work we have employed four powerful analysis tools to investigate a recently reported green-light TADF emitter, *m*-Cz-BNCz. The ALMO-based orbital interaction analysis reveals that the elevation of HOMO energy due to the anti-bonding mixing of the HOMOs of 3,6-di-*t*-butyl-Cz and BNCz is responsible for the red shift in the emission wavelength (from blue to green), which contrasts with the case of *p*-Cz-BNCz whose HOMO is almost entirely localized on the BNCz moiety. The consistent trends in the frontier orbital gaps and emission wavelengths are further reassured by the results of our excitation energy component analysis. And the two-electron components are crucial for the S_1–T_1 gaps. The charge-transfer number analysis shows that the S_1 and T_1 excited states of *m*-Cz-BNCz possess mixed LE/CT characters, wherein the contributions from the Cz → BNCz CT are 27% and 12%, respectively, while for *p*-Cz-BNCz both the S_1 and T_1 states are dominated by local excitations on the BNCz moiety. The mixed LE/CT nature of these states offers a desirable balance between a small S_1–T_1 gap and a substantial fluorescence intensity for *m*-Cz-BNCz, and the notable difference in the relative weights of CT can potentially lead to larger spin-orbit coupling between the S_1 and T_1 states and thereby facilitate efficient RISC. Finally, analysis of the vibrational reorganization energies for these two molecules reveals the extra flexibility of the structure of *m*-Cz-BNCz compared to its para-substituted counterpart arising from the torsion motion between the former's BNCz and Cz moieties, which is related to the more significant CT character of *m*-Cz-BNCz's S_1 state and gives rise to its broader and bathochromically shifted emission peak than that of *p*-Cz-BNCz. These results have demonstrated that these analysis tools are well-suited for elucidating the structure-property relationship of TADF emitters, suggesting that they should be more widely used in computational modeling and rational design of functional molecules possessing attractive photophysical properties.

Supplementary Material

Refer to Web version on PubMed Central for supplementary material.

Acknowledgement

YS is supported by the National Institutes of Health (grant: R01GM135392), Oklahoma Center for the Advancement of Science and Technology (grant: HR18-130), and the Office of the Vice President of Research and the College of Art and Sciences at the University of Oklahoma (OU). WL acknowledges financial support from the National Natural Science Foundation of China (Grant Nos. 21573177 and 21833006). ZS acknowledges financial support from the National Natural Science Foundation of China (Grant No. 21788102) as well as the Ministry of Science and Technology of China through the National Key R&D Plan (Grant No. 2017YFA0204501). QO

acknowledges financial support from the National Natural Science Foundation of China (Grant No. 22003030) as well as China Postdoctoral Science Foundation Grant No. 2020M670280. QO is also supported by the Shuimu Tsinghua Scholar Program.

References

(1). Uoyama H; Goushi K; Shizu K; Nomura H; Adachi C Highly Efficient Organic Light-Emitting Diodes from Delayed Fluorescence. Nature 2012, 492, 234–238. [PubMed: 23235877]

(2). Tao Y; Yuan K; Chen T; Xu P; Li H; Chen R; Zheng C; Zhang L; Huang W Thermally Activated Delayed Fluorescence Materials Towards the Breakthrough of Organoelectronics. Adv. Mater 2014, 26, 7931–7958. [PubMed: 25230116]

(3). Yang Z; Mao Z; Xie Z; Zhang Y; Liu S; Zhao J; Xu J; Chi Z; Aldred MP Recent Advances in Organic Thermally Activated Delayed Fluorescence Materials. Chem. Soc. Rev 2017, 46, 915–1016. [PubMed: 28117864]

(4). Godumala M; Choi S; Cho MJ; Choi DH Recent Breakthroughs in Thermally Activated Delayed Fluorescence Organic Light Emitting Diodes Containing Non-Doped Emitting Layers. J. Mater. Chem. C 2019, 7, 2172–2198.

(5). Im Y; Kim M; Seo YJCJ-A; Yook KS; Lee JY Molecular Design Strategy of Organic Thermally Activated Delayed Fluorescence Emitters. Chem. Mater 2017, 29, 1946–1863.

(6). Lee K; Kim D Local-Excitation versus Charge-Transfer Characters in the Triplet State: Theoretical Insight into the SingletTriplet Energy Differences of Carbazolyl-Phthalonitrile-Based Thermally Activated Delayed Fluorescence Materials. J. Phys. Chem. C 2016, 120, 28330–28336.

(7). Samanta PK; Kim D; Coropceanu V; Brdas J-L Up-Conversion Intersystem Crossing Rates in Organic Emitters for Thermally Activated Delayed Fluorescence: Impact of the Nature of Singlet vs Triplet Excited States. J. Am. Chem. Soc 2017, 139, 4042–4051. [PubMed: 28244314]

(8). Chen X-K; Kim D; Brdas J-L Thermally Activated Delayed Fluorescence (TADF) Path toward Efficient Electroluminescence in Purely Organic Materials: Molecular Level Insight. Acc. Chem. Res 2018, 51, 2215–2224. [PubMed: 30141908]

(9). Zhang Q; Li J; Shizu K; Huang S; Hirata S; Miyazaki H; Adachi C Design of Efficient Thermally Activated Delayed Fluorescence Materials for Pure Blue Organic Light Emitting Diodes. J. Am. Chem. Soc 2012, 134, 14706–14709. [PubMed: 22931361]

(10). Lee J; Shizu K; Tanaka H; Nakanotani H; Yasuda T; Kaji H; Adachi C Controlled Emission Colors and SingletTriplet Energy Gaps of Dihydrophenazine-Based Thermally Activated Delayed Fluorescence Emitters. J. Mater. Chem. C 2015, 3, 2175–2181.

(11). Dias FB; Penfold TJ; Monkman AP Photophysics of Thermally Activated Delayed Fluorescence Molecules. Methods Appl. Fluoresc 2017, 5, 012001. [PubMed: 28276340]

(12). Montanaro S; Gillett AJ; Feldmann S; Evans EW; Plasser F; Friend RH; Wright IA Red-Shifted Delayed Fluorescence at the Expense of Photoluminescence Quantum Efficiency an Intramolecular Charge-Transfer Molecule Based on a Benzodithiophene-4,8-dione Acceptor. Phys. Chem. Chem. Phys 2019, 21, 10580–10586. [PubMed: 31074469]

(13). Yang T; Cheng Z; Li Z; Liang J; Xu Y; Li C; Wang Y Improving the Efficiency of Red Thermally Activated Delayed Fluorescence Organic Light-Emitting Diode by Rational Isomer Engineering. Adv. Funct. Mater 2020, 30, 2002681.

(14). Rajamalli P; Senthilkumar N; Gandeepan P; Huang P-Y; Huang M-J; Ren-Wu C-Z; Yang C-Y; Chiu M-J; Chu L-K; Lin H-W et al. A New Molecular Design Based on Thermally Activated Delayed Fluorescence for Highly Efficient Organic Light Emitting Diodes. J. Am. Chem. Soc 2016, 138, 628–634. [PubMed: 26709617]

(15). Park IS; Matsuo K; Aizawa N; Yasuda T High-Performance Dibenzoheteraborin-Based Thermally Activated Delayed Fluorescence Emitters: Molecular Architectonics for Concurrently Achieving Narrowband Emission and Efficient TripletSinglet Spin Conversion. Adv. Funct. Mater 2018, 28, 1802031.

(16). Lee SY; Yasuda T; Yang YS; Zhang Q; Adachi C Luminous Butterflies: Efficient Exciton Harvesting by Benzophenone Derivatives for Full-Color Delayed Fluorescence OLEDs. Angew. Chem. Int. Ed 2014, 53, 6402–6406.

(17). Mamada M; Tian G; Nakanotani H; Su J; Adachi C The Importance of Excited-State Energy Alignment for Efficient Exciplex Systems Based on a Study of Phenylpyridinato Boron Derivatives. Angew. Chem. Int. Ed 2018, 57, 12380–12384.

(18). Hatakeyama T; Shiren K; Nakajima K; Nomura S; Nakatsuka S; Kinoshita K; Ni J; Ono Y; Ikuta T Ultrapure Blue Thermally Activated Delayed Fluorescence Molecules: Efficient HOMOLUMO Separation by the Multiple Resonance Effect. Adv. Mater 2016, 28, 2777–2781. [PubMed: 26865384]

(19). Liang X; Yan Z-P; Han H-B; Wu Z-G; Zheng Y-X; Meng H; Zuo J-L; Huang W Peripheral Amplification of Multi-Resonance Induced Thermally Activated Delayed Fluorescence for Highly Efficient OLEDs. Angew. Chem. Int. Ed 2018, 57, 11316–11320.

(20). Han SH; Jeong JH; Yoo JW; Lee JY Ideal blue thermally activated delayed fluorescence emission assisted by a thermally activated delayed fluorescence assistant dopant through a fast reverse intersystem crossing mediated cascade energy transfer process. J. Mater. Chem. C 2019, 7, 3082–3089.

(21). Matsui K; Oda S; Yoshiura K; Nakajima K; Yasuda N; Hatakeyama T One-Shot Multiple Borylation toward BN-Doped Nanographenes. J. Am. Chem. Soc 2018, 140, 1195–1198. [PubMed: 29120174]

(22). Kondo Y; Yoshiura K; Kitera S; Nishi H; Oda S; Gotoh H; Sasada Y; Yanai M; Hatakeyama T Narrowband Deep-Blue Organic Light-Emitting Diode Featuring an Organoboron-Based Emitter. Nat. Photonics 2019, 13, 678–682.

(23). Xu Y; Cheng Z; Li Z; Liang B; Wang J; Wei J; Zhang Z; Wang Y Molecular-Structure and Device-Configuration Optimizations toward Highly Efficient Green Electroluminescence with Narrowband Emission and High Color Purity. Adv. Optical Mater 2020, 8, 1902142.

(24). Xu Y; Li C; Li Z; Wang Q; Cai X; Wei J; Wang Y Constructing Charge-Transfer Excited States Based on Frontier Molecular Orbital Engineering: Narrowband Green Electroluminescence with High Color Purity and Efficiency. Angew. Chem. Int. Ed 2020, 59, 17442–17446.

(25). Mao Y; Head-Gordon M; Shao Y Unraveling Substituent Effects on Frontier Orbitals of Conjugated Molecules Using an Absolutely Localized Molecular Orbital Based Analysis. Chem. Sci 2018, 9, 8598–8607. [PubMed: 30568785]

(26). Khaliullin RZ; Head-Gordon M; Bell AT An Efficient Self-Consistent Field Method for Large Systems of Weakly Interacting Components. J. Chem. Phys 2006, 124, 204105. [PubMed: 16774317]

(27). Khaliullin RZ; Cobar EA; Lochan RC; Bell AT; Head-Gordon M Unravelling the Origin of Intermolecular Interactions Using Absolutely Localized Molecular Orbitals. J. Phys. Chem. A 2007, 111, 8753–8765. [PubMed: 17655284]

(28). Khaliullin RZ; Bell AT; Head-Gordon M Analysis of Charge Transfer Effects in Molecular Complexes Based on Absolutely Localized Molecular Orbitals. J. Chem. Phys 2008, 128, 184112. [PubMed: 18532804]

(29). Horn PR; Mao Y; Head-Gordon M Probing Non-covalent Interactions with a Second Generation Energy Decomposition Analysis Using Absolutely Localized Molecular Orbitals. Phys. Chem. Chem. Phys 2016, 18, 23067–23079. [PubMed: 27492057]

(30). Mao Y; Horn PR; Head-Gordon M Energy Decomposition Analysis in an Adiabatic Picture. Phys. Chem. Chem. Phys 2017, 19, 5944–5958. [PubMed: 28176997]

(31). Mo Y; Gao J; Peyerimhoff SD Energy Decomposition Analysis of Intermolecular Interactions Using a Block-Localized Wave Function Approach. J. Chem. Phys 2000, 112, 5530–5538.

(32). Mo Y; Gao J Theoretical Analysis of the Rotational Barrier of Ethane. Acc. Chem. Res 2007, 40, 113–119. [PubMed: 17309192]

(33). Mo Y; Bao P; Gao J Energy Decomposition Analysis Based on a Block-Localized Wavefunction and Multistate Density Functional Theory. Phys. Chem. Chem. Phys 2011, 13, 6760. [PubMed: 21369567]

(34). Zhang H; Jiang X; Wu W; Mo Y Electron Conjugation versus pipi Repulsion in Substituted Benzenes: Why the CarbonNitrogen Bond in Nitrobenzene is Longer Than in Aniline. Phys. Chem. Chem. Phys 2016, 18, 11821–11828. [PubMed: 26852720]

(35). Shao Y; Gan Z; Epifanovsky E; Gilbert AT; Wormit M; Kussmann J; Lange AW; Behn A; Deng J; Feng X et al. Advances in Molecular Quantum Chemistry Contained in the Q-Chem 4 Program Package. Mol. Phys 2015, 113, 184–215.

(36). Henderson TM; Janesko BG; Scuseria GE Generalized Gradient Approximation Model Exchange Holes for Range-Separated Hybrids. J. Chem. Phys 2008, 128, 194105. [PubMed: 18500854]

(37). Rohrdanz MA; Martins KM; Herbert JM A Long-Range-Corrected Density Functional That Performs Well for both Ground-State Properties and Time-Dependent Density Functional Theory Excitation Energies, Including Charge-Transfer Excited States. J. Chem. Phys 2009, 130, 054112. [PubMed: 19206963]

(38). Kronik L; Stein T; Refaely-Abramson S; Baer R Excitation Gaps of Finite-Sized Systems from Optimally Tuned Range-Separated Hybrid Functionals. J. Chem. Theory Comput 2012, 8, 1515–1531, PMID: 26593646. [PubMed: 26593646]

(39). Sun H; Zhong C; Brdas J-L Reliable Prediction with Tuned Range-Separated Functionals of the SingletTriplet Gap in Organic Emitters for Thermally Activated Delayed Fluorescence. J. Chem. Theory Comput 2015, 11, 3851–3858. [PubMed: 26574466]

(40). Shee J; Head-Gordon M Predicting Excitation Energies of Twisted Intramolecular Charge-Transfer States with the Time-Dependent Density Functional Theory: Comparison with Experimental Measurements in the Gas Phase and Solvents Ranging from Hexanes to Acetonitrile. J. Chem. Theory Comput 2020, 16, 6244–6255. [PubMed: 32816472]

(41). Head-Gordon M; Maslen PE; White CA A Tensor Formulation of Many-Electron Theory in a Nonorthogonal Single-Particle Basis. J. Chem. Phys 1998, 108, 616–625.

(42). Kimber P; Plasser F Toward an Understanding of Electronic Excitation Energies Beyond the Molecular Orbital Picture. Phys. Chem. Chem. Phys 2020, 22, 6058–6080. [PubMed: 32154539]

(43). Pei Z; Yang J; Deng J; Mao Y; Wu Q; Yang Z; Wang B; Aikens CM; Liang W; Shao Y Analysis and Visualization of Energy Densities. II. Insights from Linear-Response Time-Dependent Density Functional Theory Calculations. Phys. Chem. Chem. Phys 2020, 22, 26852–26864. [PubMed: 33216085]

(44). It should be noted that the computational S_1–T_1 energy gap here is obtained at the S_0 optimized geometry. Such vertical energy gap is expected to be lager than the experimental result, which indeed corresponds to the adiabatic energy gap between S_1 and T_1 with zero-point vibrational energy correction that takes geometry relaxation into accounts.

(45). Kim D Effects of Intermolecular Interactions on the SingletTriplet Energy Difference: A Theoretical Study of the Formation of Excimers in Acene Molecules. J. Phys. Chem. C 2015, 119, 12690–12697.

(46). Plasser F; Wormit M; Dreuw A New Tools for the Systematic Analysis and Visualization of Electronic Excitations. I. Formalism. J. Chem. Phys 2014, 141, 024106. [PubMed: 25027998]

(47). Plasser F TheoDORE: A toolbox for a Detailed and Automated Analysis of Electronic Excited State Computations. J. Chem. Phys 2020, 152, 084108. [PubMed: 32113349]

(48). Mewes SA; Plasser F; Dreuw A Universal Exciton Size in Organic Polymers is Determined by Nonlocal Orbital Exchange in Time-Dependent Density Functional Theory. J. Phys. Chem. Lett 2017, 8, 1205–1210. [PubMed: 28230997]

(49). Pinheiro M; Machado FBC; Plasser F; Aquino AJA; Lischka H A Systematic Analysis of Excitonic Properties to Seek Optimal Singlet Fission: the BN-substitution Patterns in Tetracene. J. Mater. Chem. C 2020, 8, 7793–7804.

(50). Mewes J-M Modeling TADF in Organic Emitters Requires a Careful Consideration of the Environment and Going Beyond the FranckCondon Approximation. Phys. Chem. Chem. Phys 2018, 20, 12454–12469. [PubMed: 29700532]

(51). Lv M; Yu Y; SandovalSalinas ME; Xu J; Lei Z; Casanova D; Yang Y; Chen J Engineering the Charge-Transfer State to Facilitate SpinOrbit Charge Transfer Intersystem Crossing in Spirobis[anthracene]diones. Angew. Chem. Int. Ed 2020, 59, 22179–22184.

(52). Gibson J; Monkman AP; Penfold TJ The Importance of Vibronic Coupling for Efficient Reverse Intersystem Crossing in Thermally Activated Delayed Fluorescence Molecules. ChemPhysChem 2016, 2956–2961. [PubMed: 27338655]

(53). De Silva P; Kim CA; Zhu T; Van Voorhis T Extracting Design Principles for Efficient Thermally Activated Delayed Fluorescence (TADF) from a Simple Four-State Model. Chem. Mater 2019, 31, 6995–7006.

(54). Niu Y; Peng Q; Deng C; Gao X; Shuai Z Theory of Excited State Decays and Optical Spectra: Application to Polyatomic Molecules. J. Phys. Chem. A 2010, 114, 7817–7831. [PubMed: 20666533]

(55). Penfold TJ; Gindensperger E; Daniel C; Marian CM Spin-Vibronic Mechanism for Intersystem Crossing. Chem. Rev 2018, 118, 6975–7025. [PubMed: 29558159]

(56). Kim I; Jeon SO; Jeong D; Choi H; Son W-J; Kim D; Rhee YM; Lee HS SpinVibronic Model for Quantitative Prediction of Reverse Intersystem Crossing Rate in Thermally Activated Delayed Fluorescence Systems. J. Chem. Theory Comput 2020, 16, 621–632. [PubMed: 31841330]

(57). Deng C; Niu Y; Peng Q; Shuai Z Electronic Structures and Spectroscopic Properties of Group-14 Metalloles MPh_6 (M=Si, Ge, Sn). Acta Phys.-Chim. Sinica 2010, 26, 1051–1058.

(58). Reimers JR A Practical Method for the Use of Curvilinear Coordinates in Calculations of Normal-Mode-Projected Displacements and Duschinsky Rotation Matrices for Large Molecules. J. Chem. Phys 2001, 115, 9103–9109.

(59). Shuai Z; Peng Q Organic Light-Emitting Diodes: Theoretical Understanding of Highly Efficient Materials and Development of Computational Methodology. Natl. Sci. Rev 2016, 4, 224–239.

(60). Peng Q; Yi Y; Shuai Z; Shao J Toward Quantitative Prediction of Molecular Fluorescence Quantum Efficiency: Role of Duschinsky Rotation. J. Am. Chem. Soc 2007, 129, 9333–9339. [PubMed: 17622142]

(61). Shuai Z Thermal Vibration Correlation Function Formalism for Molecular Excited State Decay Rates. Chin. J. Chem 2020, 38, 1223–1232.

(62). You Z-Q; Mewes J-M; Dreuw A; Herbert JM Comparison of the Marcus and Pekar Partitions in the Context of Non-Equilibrium, Polarizable-Continuum Solvation Models. J. Chem. Phys 2015, 143, 204104. [PubMed: 26627947]

(63). Pershin A; Hall D; Lemaur V; Sancho-Garcia J-C; Muccioli L; Zysman-Colman E; Beljonne D; Olivier Y Highly Emissive Excitons with Reduced Exchange Energy in Thermally Activated Delayed Fluorescent Molecules. Nat. Commun 2019, 10, 597. [PubMed: 30723203]

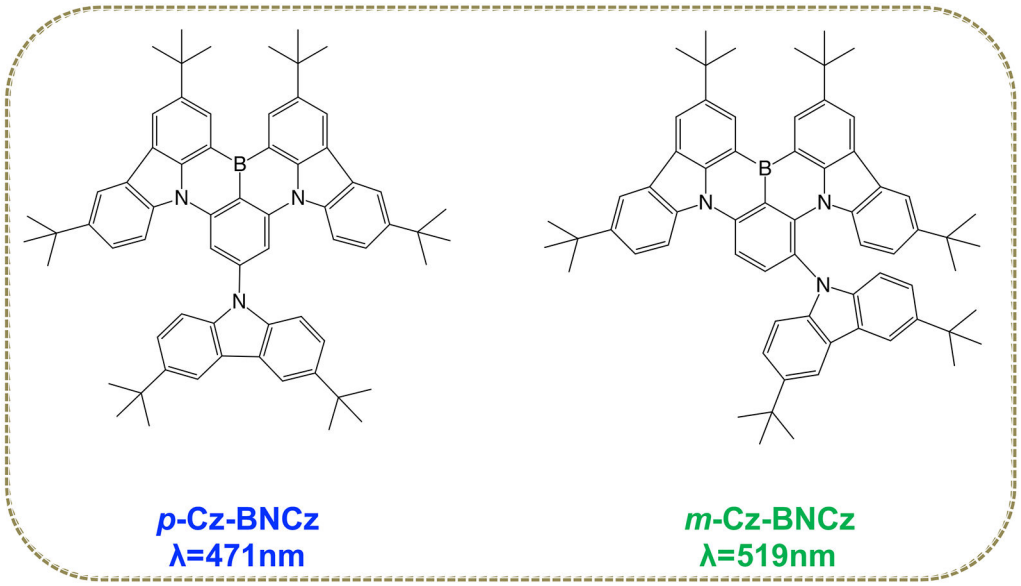

Figure 1:

Molecular structures of the green TADF emitter, *m*-Cz-BNCz, and its para-substituted isomer, *p*-Cz-BNCz, which emits blue light. The experimental emission wavelengths are obtained from Ref. 24.

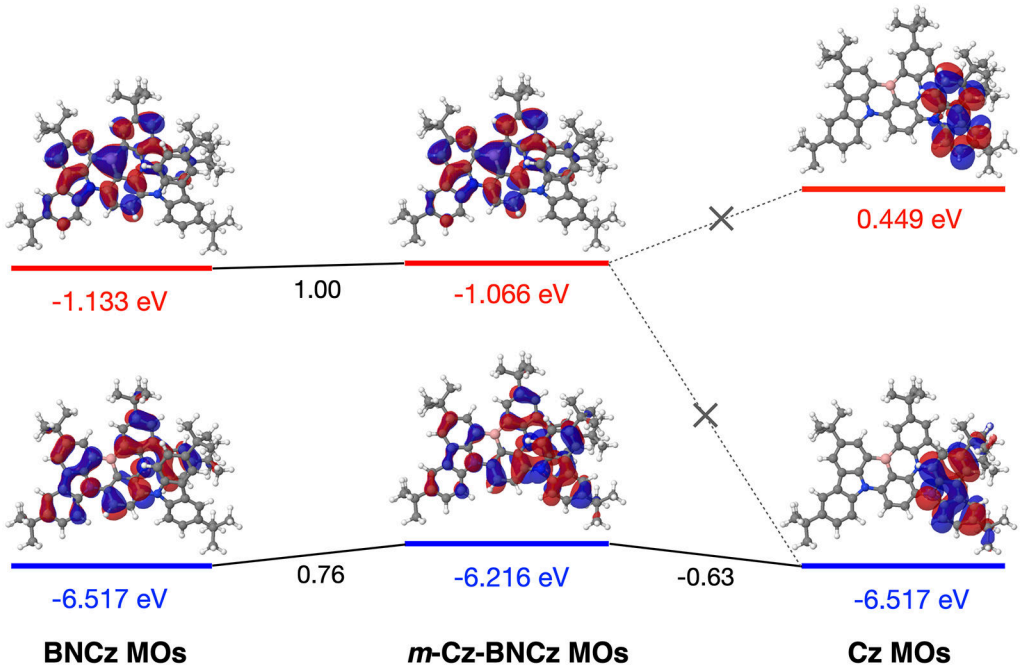

Figure 2:

ALMO analysis of the interactions between BNCz and Cz frontier orbitals to produce the fully converged MOs of *m*-Cz-BNCz complex using the LRC-ωPBE functional with an optimally tuned ω value of 0.136 a_0^{-1} and 6-311G(d,p) basis set. All orbital energies are in eV. An isovalue of 0.02 a.u. is used for the MO plots. Numerical values in black refer to projection coefficients, which are calculated based on Eq. 2.

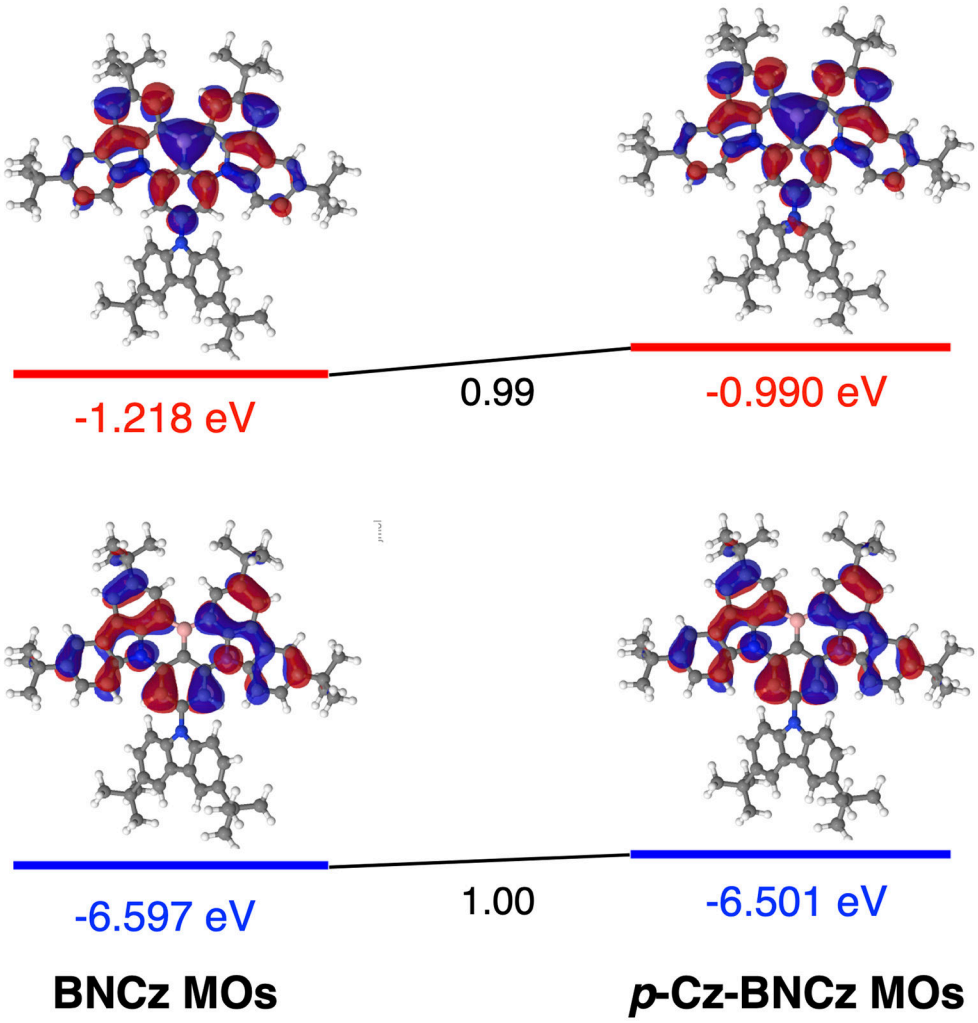

Figure 3:

ALMO analysis of the interactions between BNCz and Cz frontier orbitals to produce the fully converged MOs of *p*-Cz-BNCz complex using the LRC-ωPBE functional with an optimally tuned ω value of 0.140 a_0^{-1} and 6-311G(d,p) basis set. All orbital energies are in eV. An isovalue of 0.02 a.u. is used for the MO plots. Numerical values in black refer to projection coefficients, which are calculated based on Eq. 2.

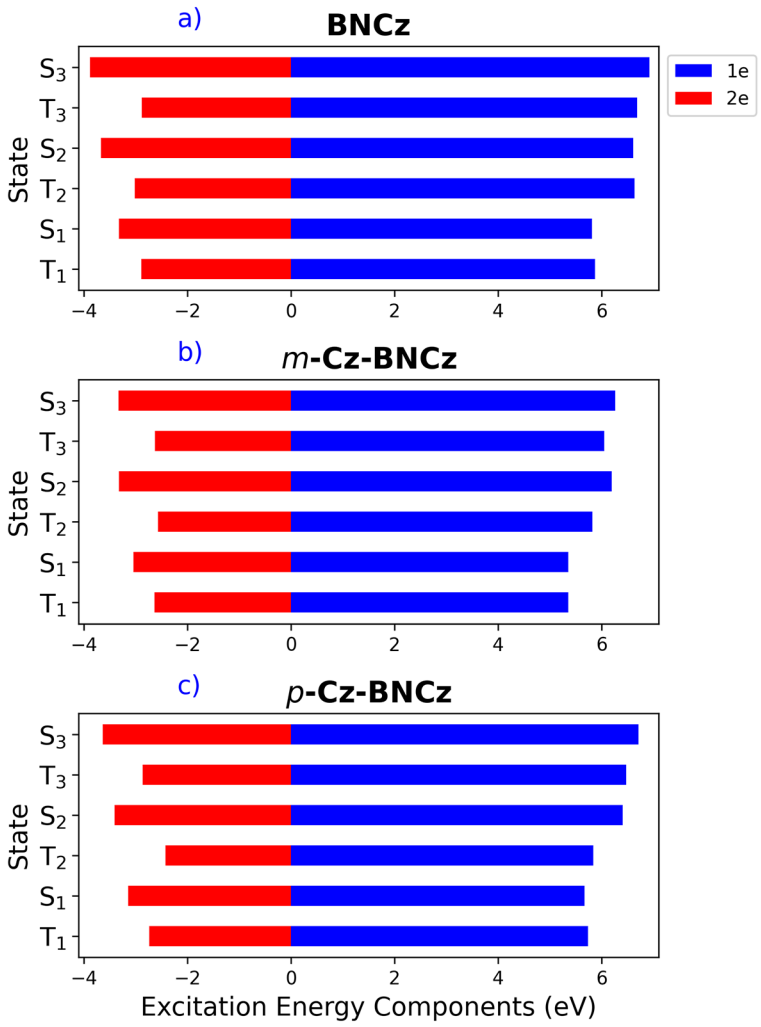

Figure 4:

Excitation energy decomposition of the first six TDDFT-TDA excited states of BNCz, *m*-Cz-BNCz, and *p*-Cz-BNCz calculated using the LRC-ωPBE functional (with ω values of 0.154 a_0^{-1}, 0.136 a_0^{-1} and 0.140 a_0^{-1}, respectively) and 6-311G(d,p) basis set.

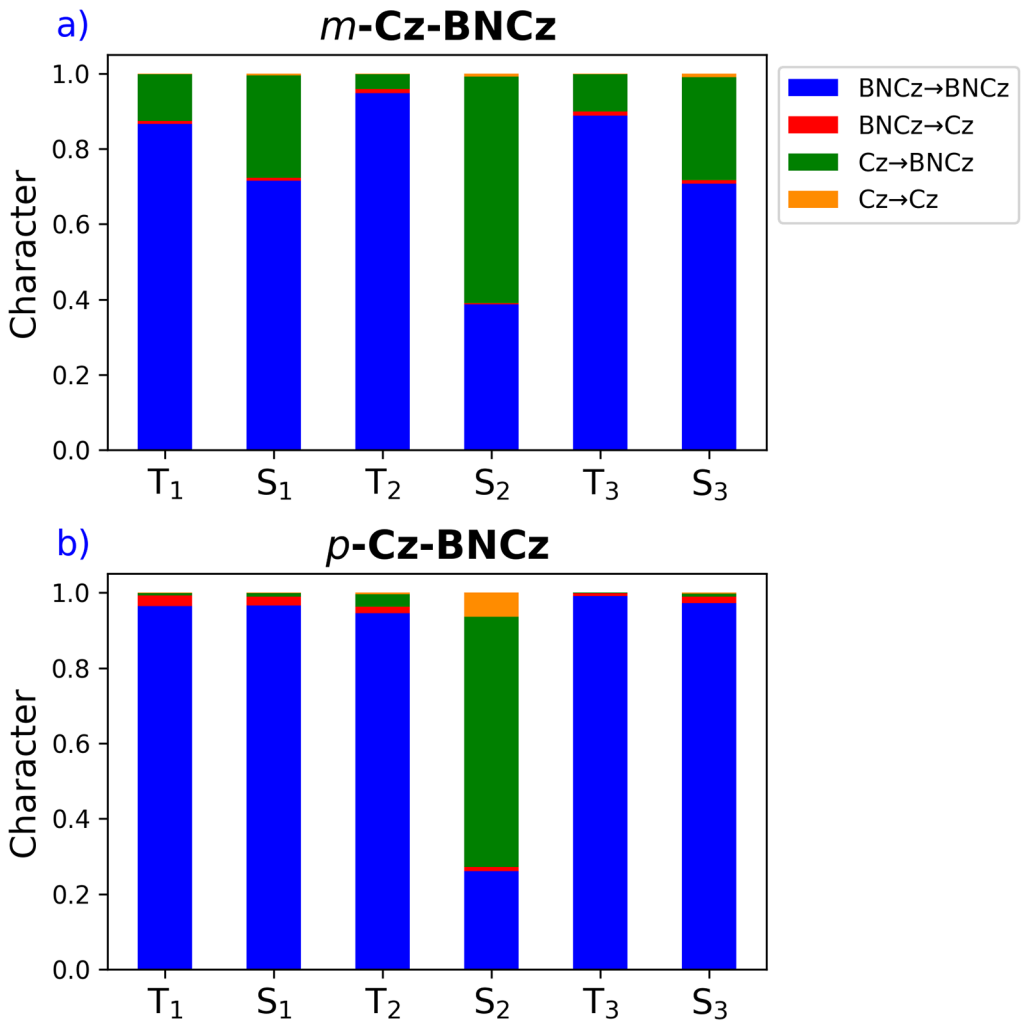

Figure 5:

Charge-transfer numbers of the first six TDDFT-TDA excited states of *m*-Cz-BNCz and *p*-Cz-BNCz calculated using the LRC-ωPBE functional (with ω values of 0.136 a_0^{-1} and 0.140 a_0^{-1}, respectively) and 6-311G(d,p) basis set. The FBH fragment partitioning scheme is used.

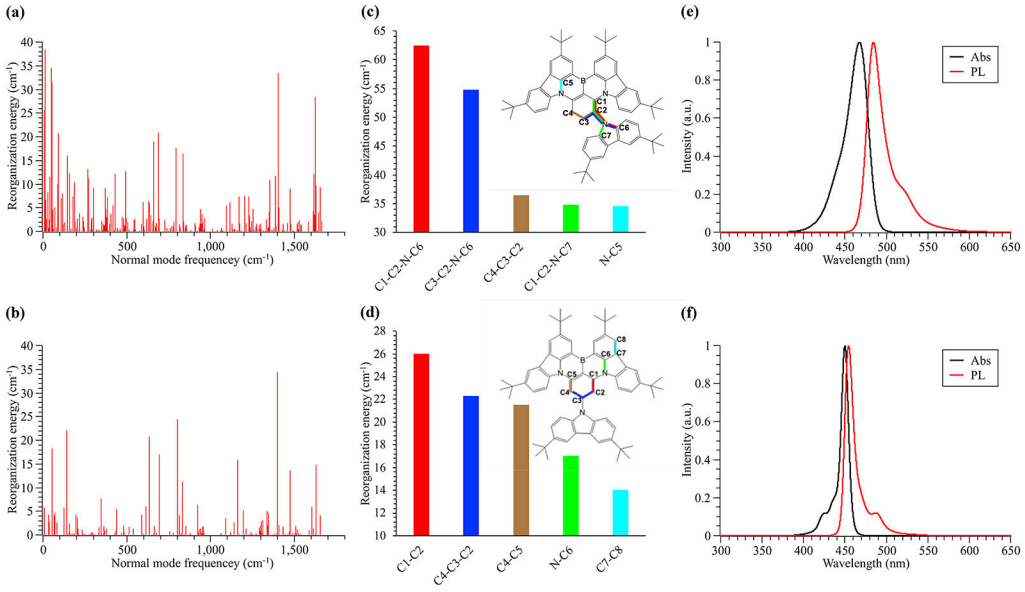

Figure 6:

Electronic vibrational coupling analysis and calculated absorption and photoluminescence spectra for *m*-Cz-BNCz and *p*-Cz-BNCz. (**a**) and (**b**) depict the reorganization energy between S_0 and S_1 at S_1-optimized geometries for *m*-Cz-BNCz and *p*-Cz-BNCz, respectively, while (**c**) and (**d**) depict the corresponding projected reorganization energy onto internal coordinates (shown with the largest five components). (**e**) and (**f**) are the absorption (Abs) and photoluminescence (PL) spectra of *m*-Cz-BNCz and *p*-Cz-BNCz computed via the TVCF formalism. Electronic vibrational coupling analysis as well as the calculation of spectra are performed with the B3LYP functional and 6-31G(d) basis set due to the limited availability of the analytical nuclear gradient and Hessian of the optimally tuned LRC-ωPBE functional.